Supporting Information

Synthesis and structural studies of 1,4-di(2-pyridyl)-1,2,3-triazole dpt and its transition metal complexes; a versatile and subtly unsymmetric ligand

Eoin P. McCarney,[a] Chris S. Hawes,[a] Salvador Blasco[a] and Thorfinnur Gunnlaugsson[a]*

[a] *School of Chemistry and Trinity Biomedical Science Institute, University of Dublin, Trinity College Dublin, Dublin 2 (Ireland)*

E-mail(s): gunnlaut@tcd.ie

Experimental

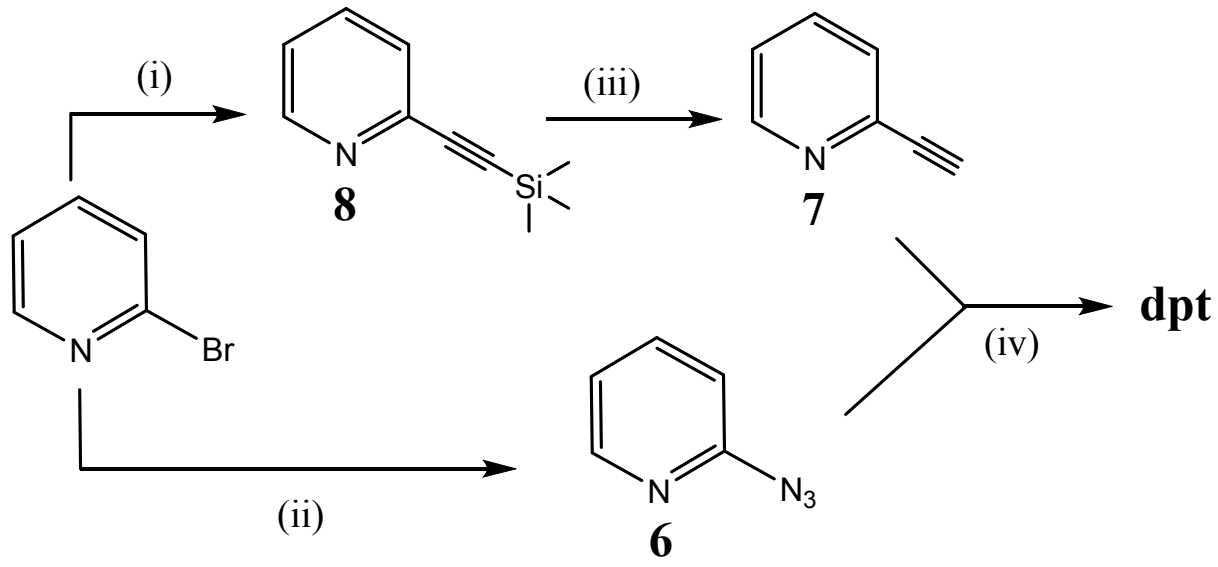

Scheme S1 – Synthetic route to **dpt:** (i) trimethylsilylacetylene $Pd(PPh_3)_2Cl_2$, CuI, Et_3N:THF, rt. (ii) N,N'-DMEDA, NaAsc, NaN_3, CuI, EtOH:H_2O. (iii) TBAF, rt. (iv) $[Cu(CH_3CN)_4]PF_6$, TBTA, Toluene, 90°C.

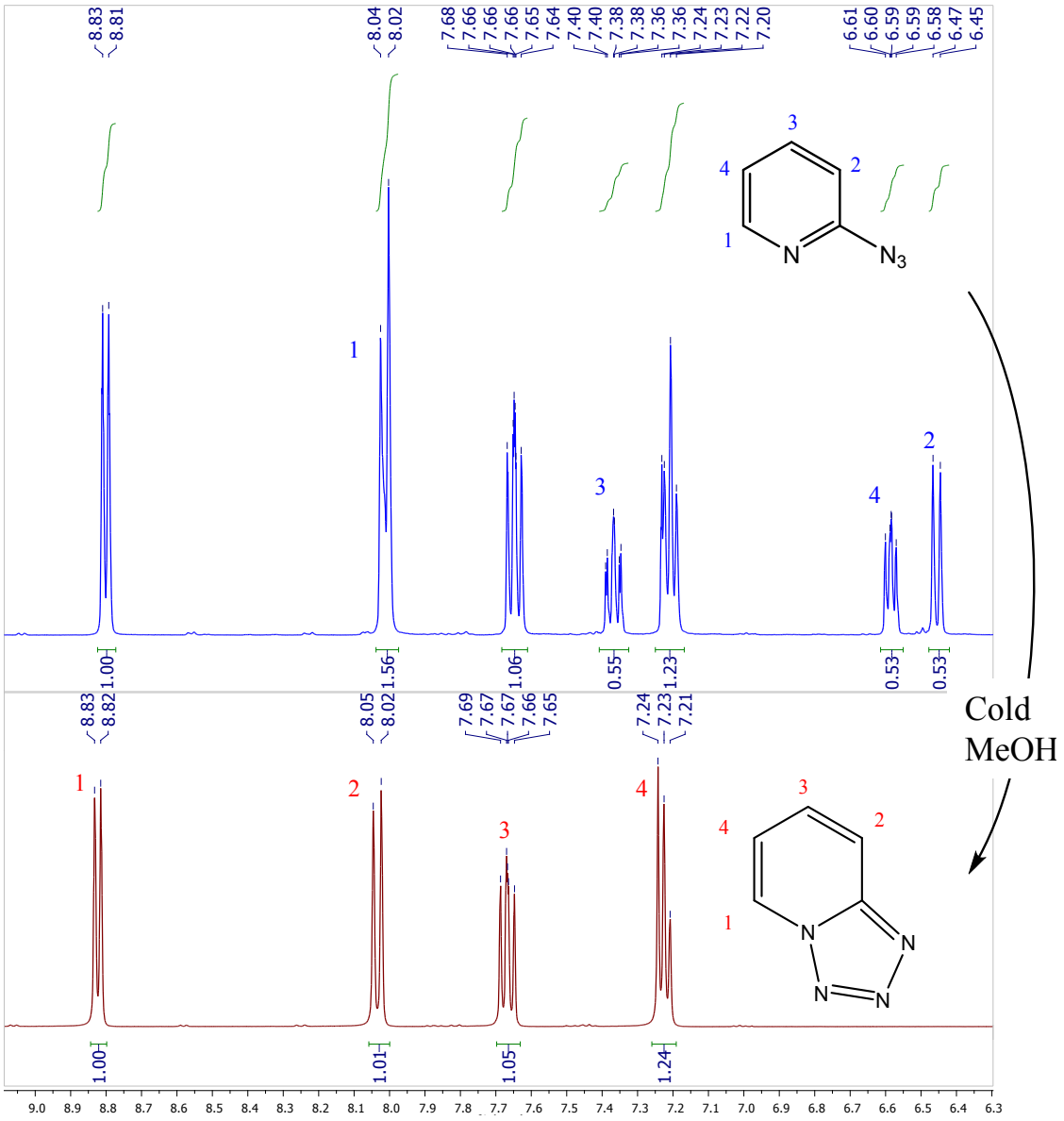

Figure S1 – ^{1}H NMR ($CDCl_3$) of **6** displaying the effect of solvent polarity on ring-tautomerisation.

It appeared that along with the peaks at 8.82 ppm, 8.03 ppm, 7.73-7.61 ppm and 7.28 – 7.18 ppm there were peaks with comparable splitting pattern occurring at 8.02 ppm, 7.40 ppm, 6.59 ppm and 6.46 ppm each in a 1:1:1:1 relative abundance to eachother. In an attempt to remove these impurity peaks, as they were considered at the time, the compound was triurated with cold CH_3OH and filtered. The ^{1}H NMR of this compound showed recovery of the signals from the inital work-up and a loss of the azide signals. There was no evidence ofcompound dissolved in the CH_3OH filtrate. The position of equilibrium is dependent on the solvent polarity and the temperature. The cold CH_3OH wash forced the equilibrium to shift in favour of the tetrazole. This explained why, in the polar DMF:H_2O mixture, the CuAAC does not occur to any noticeable extent.

(A)

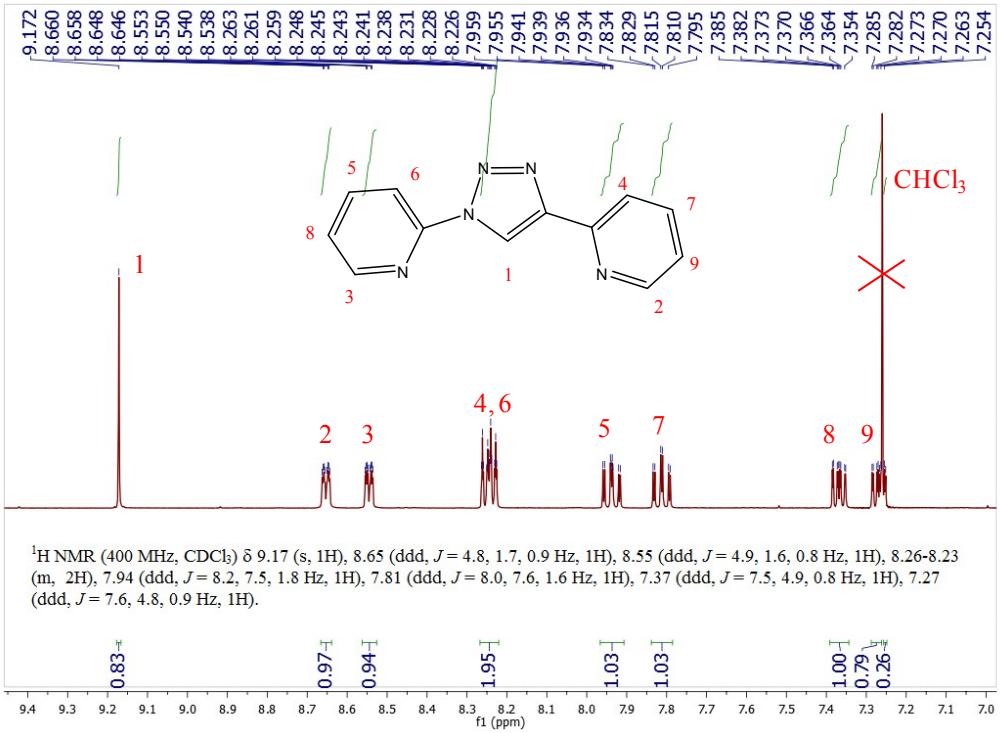

^{1}H NMR (400 MHz, $CDCl_3$) δ 9.17 (s, 1H), 8.65 (ddd, J = 4.8, 1.7, 0.9 Hz, 1H), 8.55 (ddd, J = 4.9, 1.6, 0.8 Hz, 1H), 8.26-8.23 (m, 2H), 7.94 (ddd, J = 8.2, 7.5, 1.8 Hz, 1H), 7.81 (ddd, J = 8.0, 7.6, 1.6 Hz, 1H), 7.37 (ddd, J = 7.5, 4.9, 0.8 Hz, 1H), 7.27 (ddd, J = 7.6, 4.8, 0.9 Hz, 1H).

(B)

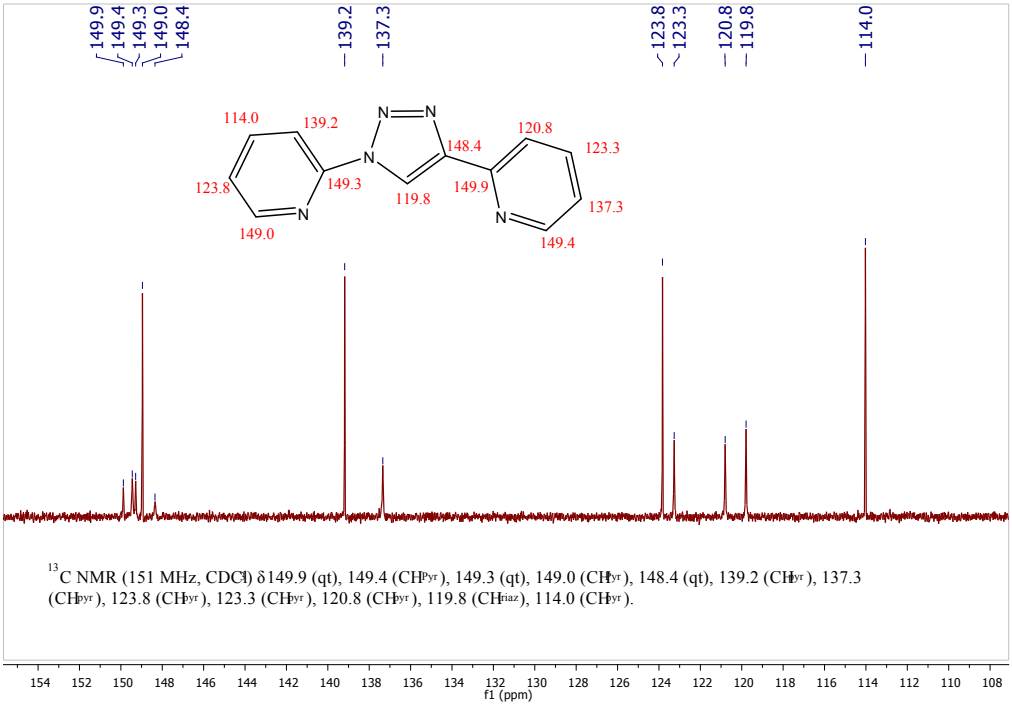

^{13}C NMR (151 MHz, $CDCl_3$) δ 149.9 (qt), 149.4 (CH^{Pyr}), 149.3 (qt), 149.0 (CH^{Pyr}), 148.4 (qt), 139.2 (CH^{Pyr}), 137.3 (CH^{Pyr}), 123.8 (CH^{Pyr}), 123.3 (CH^{Pyr}), 120.8 (CH^{Pyr}), 119.8 (CH^{triaz}), 114.0 (CH^{Pyr}).

Figure S2 - (A) ^{1}H NMR of **dpt** (600 MHz, $CDCl_3$), **(B)** ^{13}C NMR of **dpt** (151 MHz, $CDCl_3$)

(A)

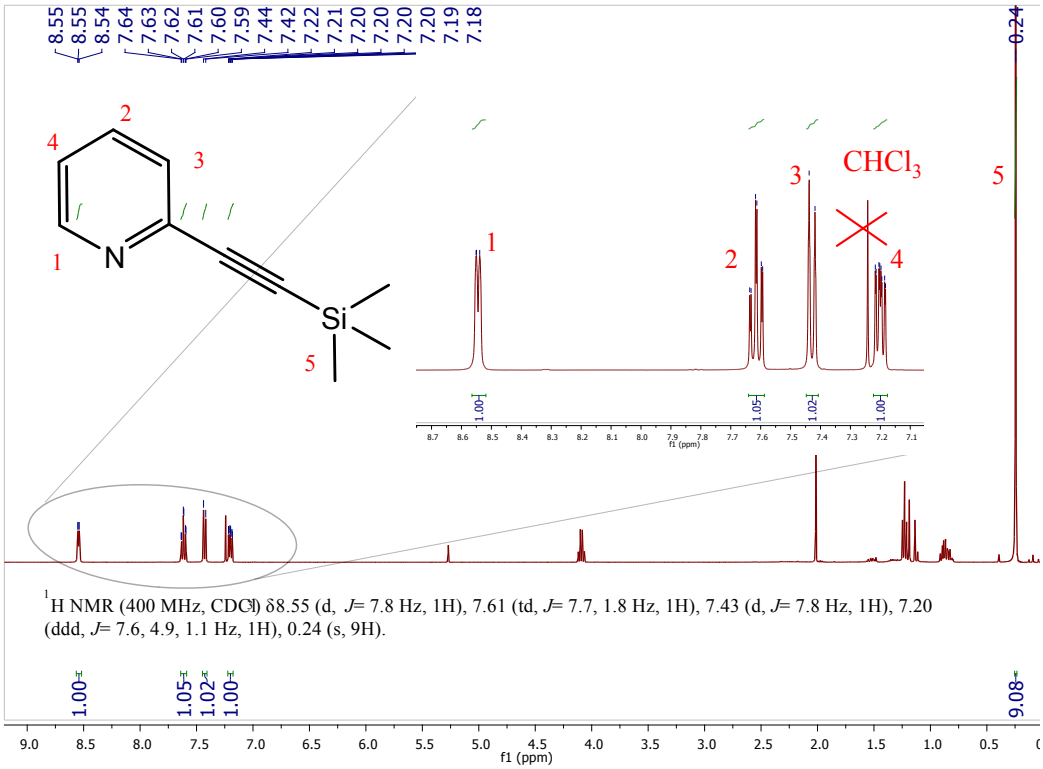

^{1}H NMR (400 MHz, CDCl$_3$) δ8.55 (d, *J*= 7.8 Hz, 1H), 7.61 (td, *J*= 7.7, 1.8 Hz, 1H), 7.43 (d, *J*= 7.8 Hz, 1H), 7.20 (ddd, *J*= 7.6, 4.9, 1.1 Hz, 1H), 0.24 (s, 9H).

(B)

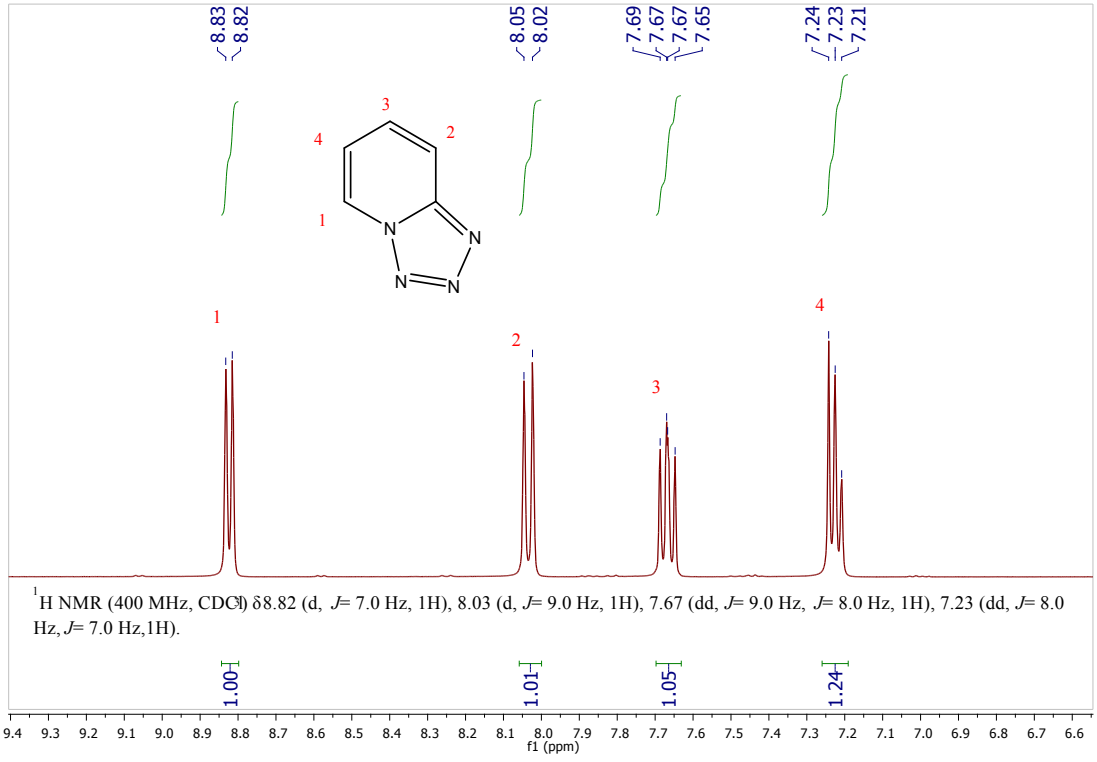

^{1}H NMR (400 MHz, CDCl$_3$) δ8.82 (d, *J*= 7.0 Hz, 1H), 8.03 (d, *J*= 9.0 Hz, 1H), 7.67 (dd, *J*= 9.0 Hz, *J*= 8.0 Hz, 1H), 7.23 (dd, *J*= 8.0 Hz, *J*= 7.0 Hz,1H).

Figure S3 - (A) ^{1}H NMR of **8** (400 MHz, $CDCl_3$), **(B)** ^{1}H NMR of **6** (400 MHz, $CDCl_3$).

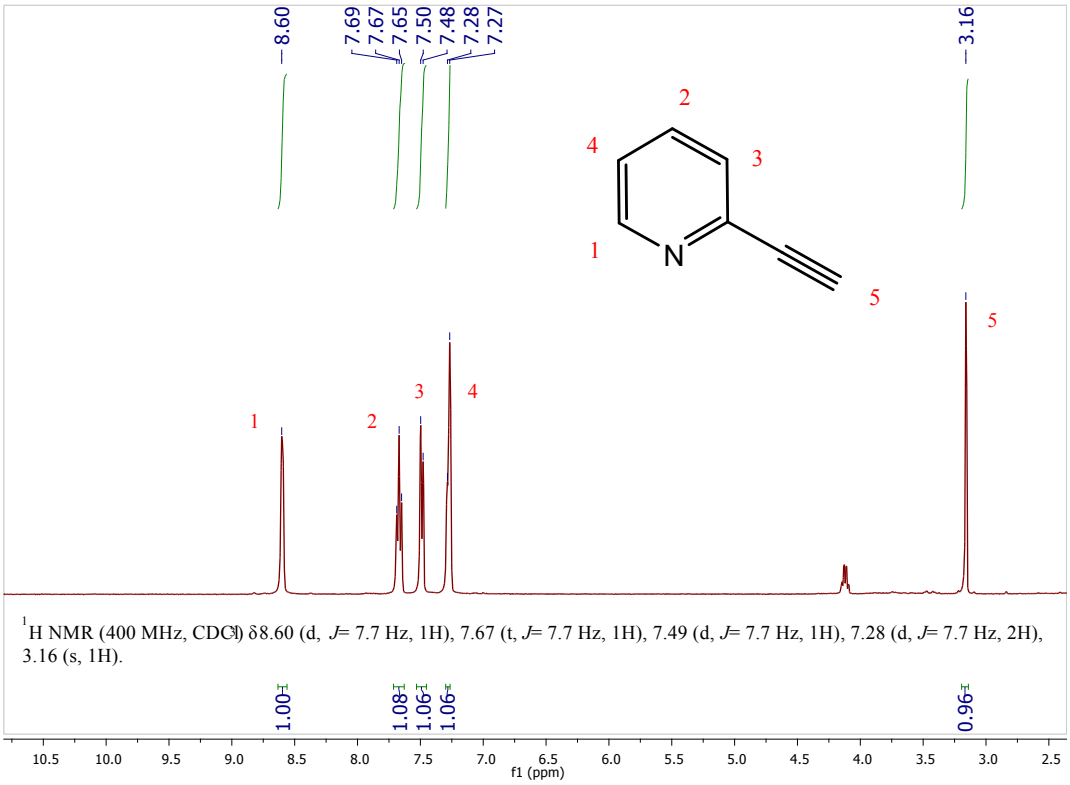

Figure S4 - ^{1}H NMR of **7** (400 MHz, $CDCl_3$

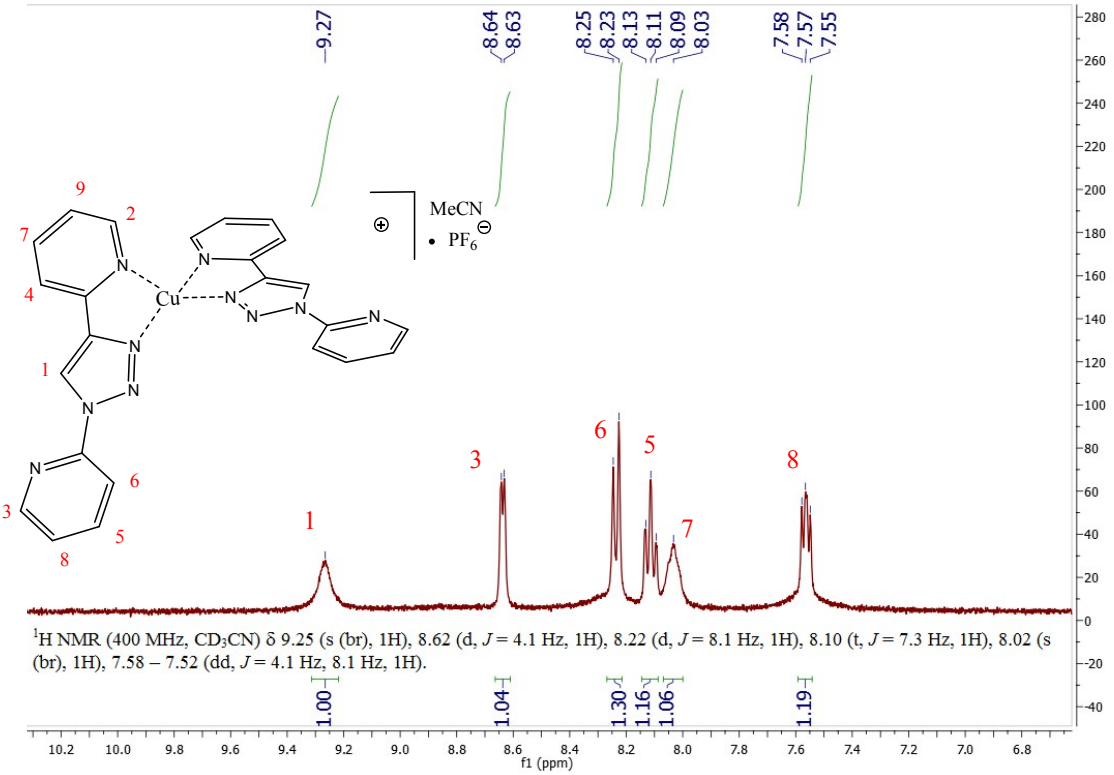

Figure S5 - ^{1}H NMR (400 MHz, CD_3CN) spectrum of **1**

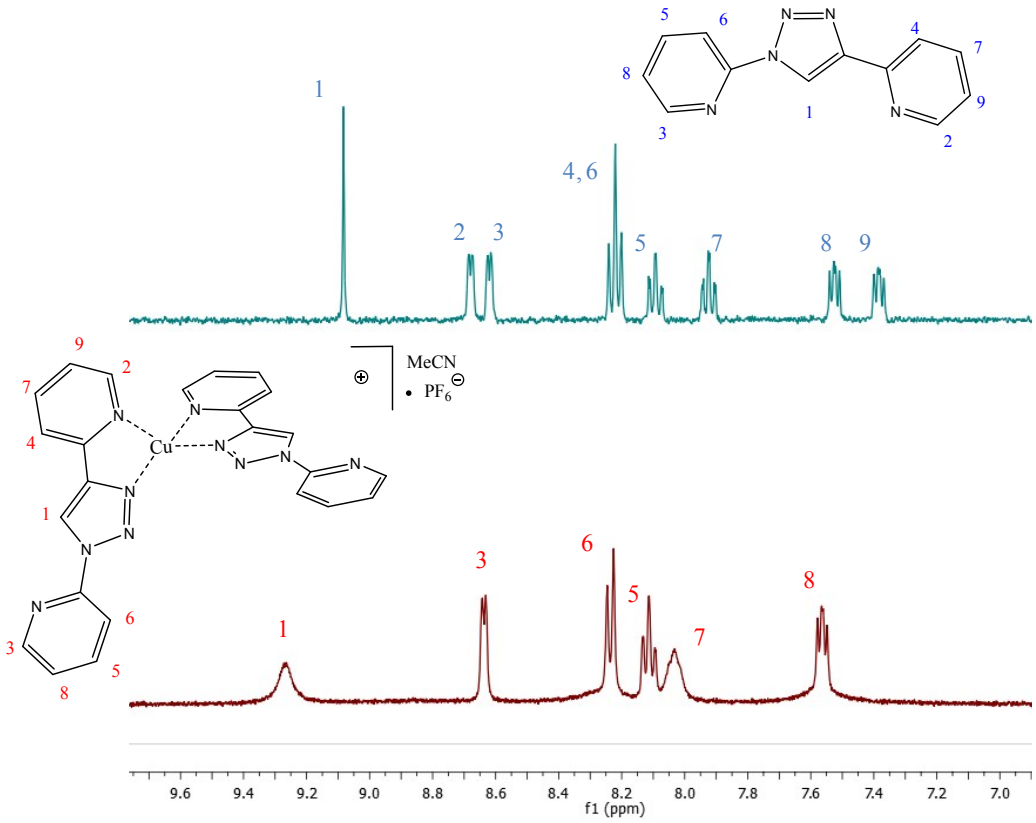

Figure S6 - ^{1}H NMR (400 MHz, CD_3CN) comparison of **dpt** (blue) and **1** (red) showing the broadening of the peaks associated with the 2-(1H-1,2,3-triazol-4-yl)pyridine (*reg*) chelate pocket.

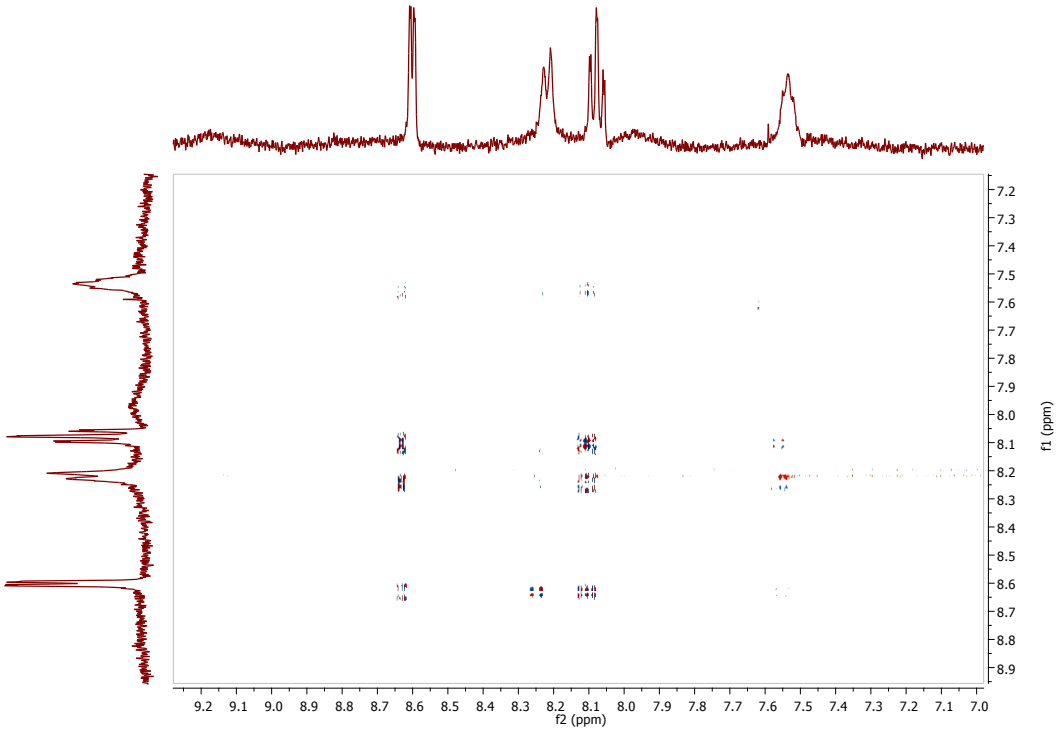

Figure S7 - ^{1}H NMR (400 MHz, CD_3CN) HH COSY of **1** showing that the sharp peaks associated with the non-chelating pyridine consisted of the one magnetically coupled ring system.

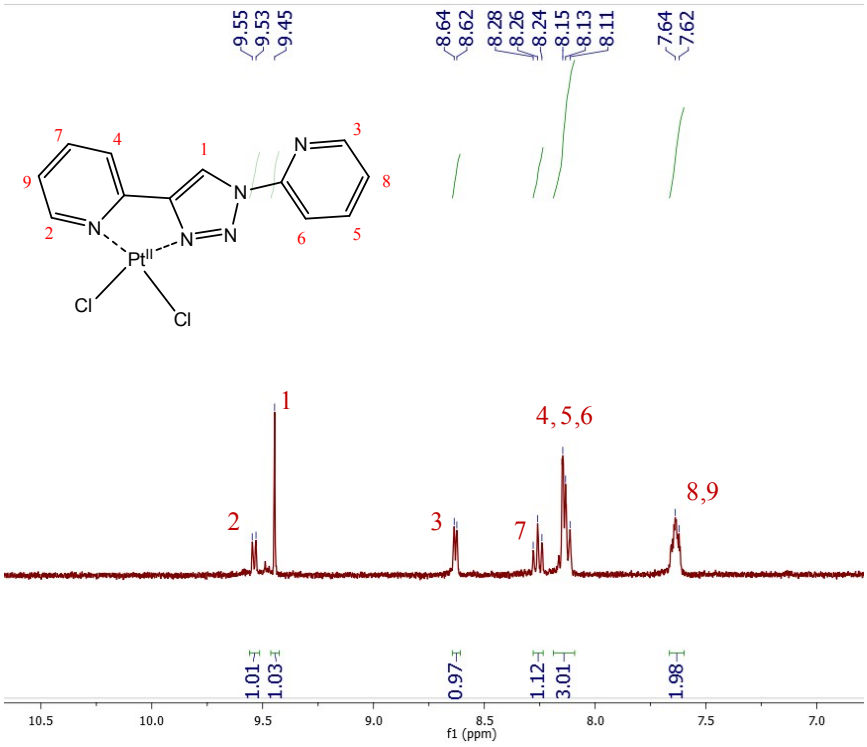

Figure S8(A) – ^{1}H NMR (CD_3CN) of **2** showing the exclusive presence of the regular isomer.

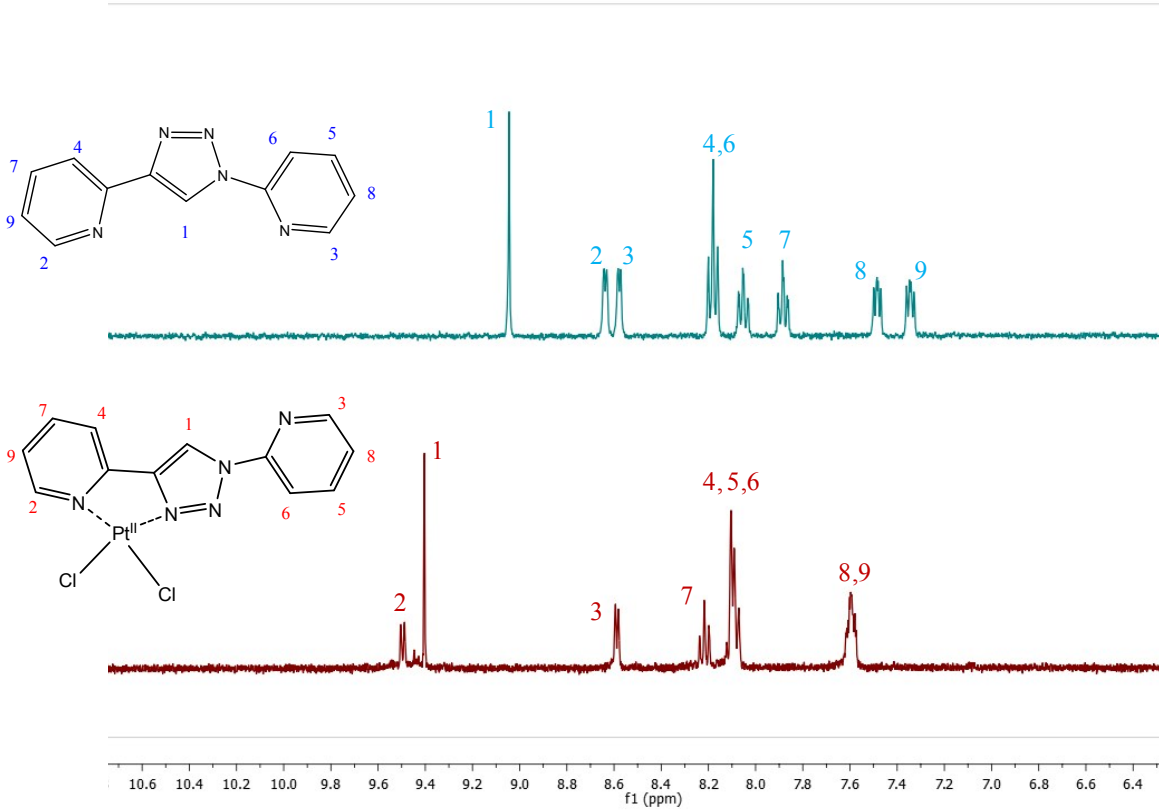

Figure S8(B) - ^{1}H NMR (CD_3CN) comparison of ligand **dpt** with complex **2**.

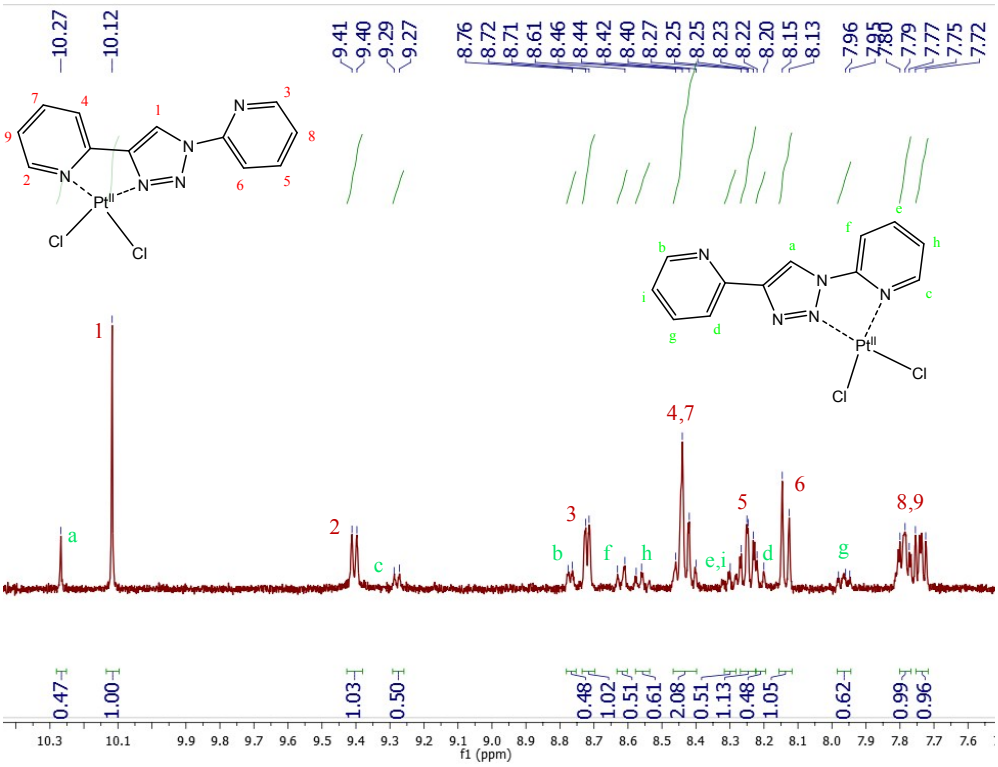

Figure S9(A) – ^{1}H NMR (DMSO-d_6) of **2** showing the *reg*:*inv* binding mode isomerism.

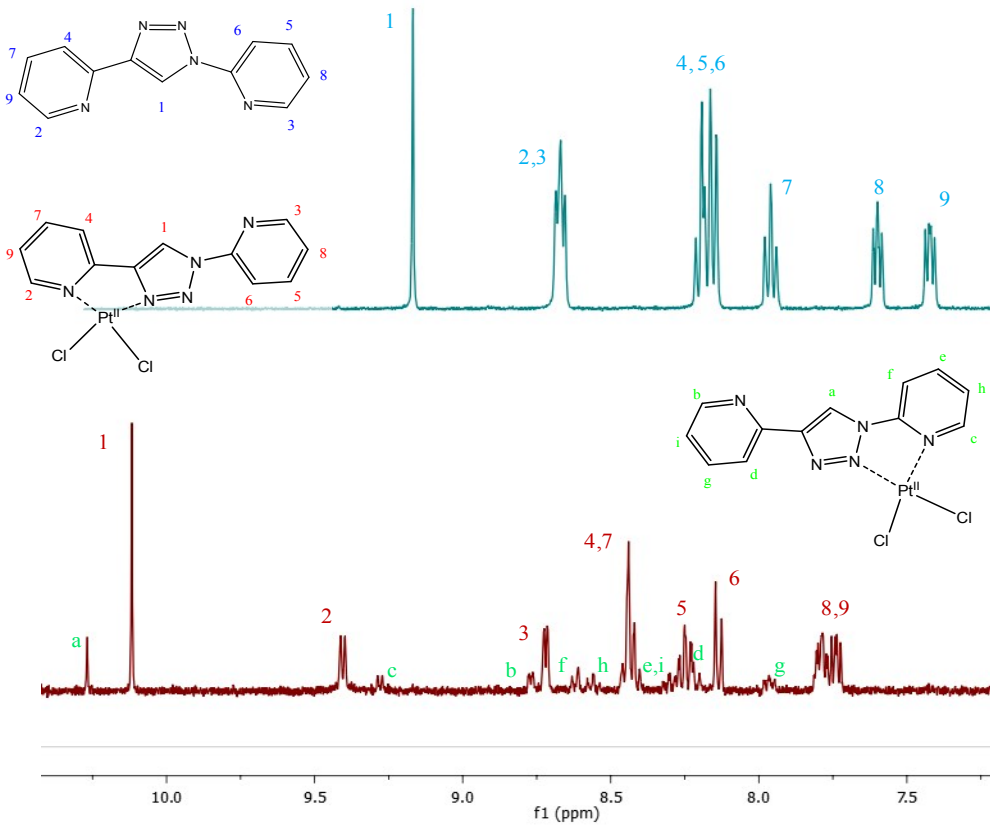

Figure S9(B) – ^{1}H NMR (DMSO-d_6) comparison of the **dpt** ligand with a mixture of both *reg* and *inv* binding modes of the [**$PtCl_2$(dpt)**] complex.

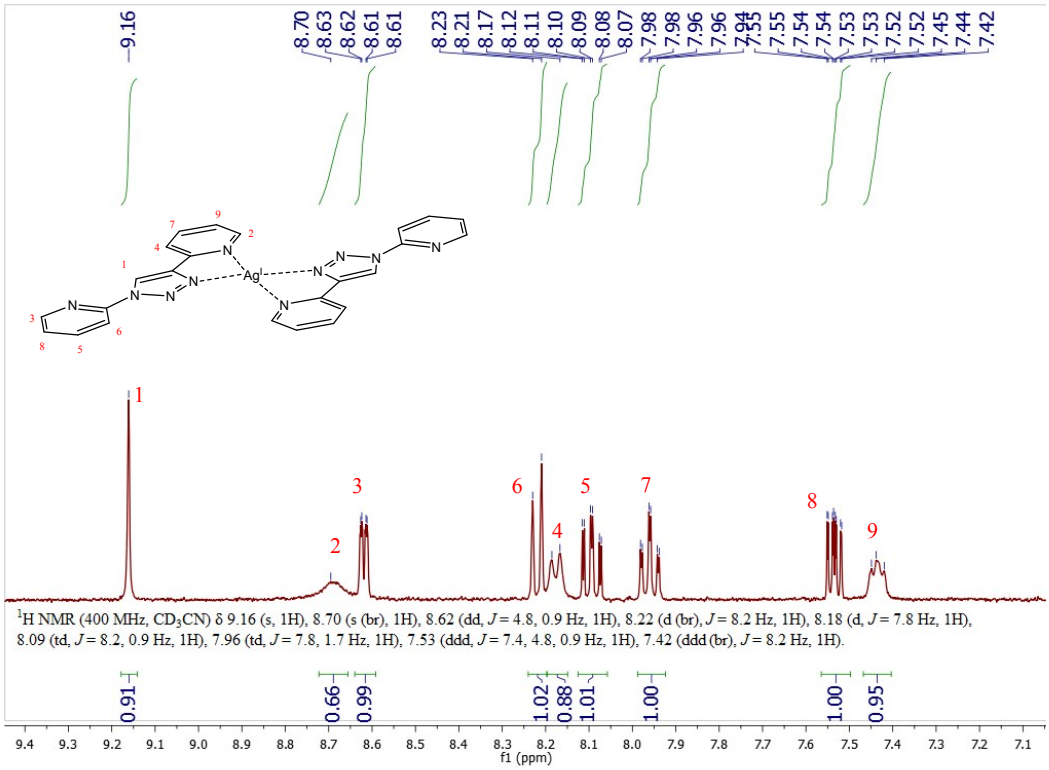

Figure S10 – ^{1}H NMR (CD$_3$CN) spectrum of **5**.

Crystallography

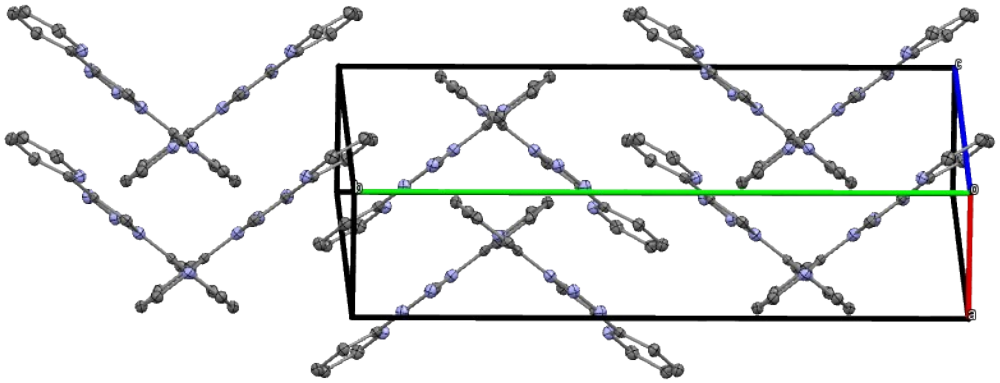

Figure S11 – Herringbone crystal packing of **dpt** with interplanar π-π stacking.

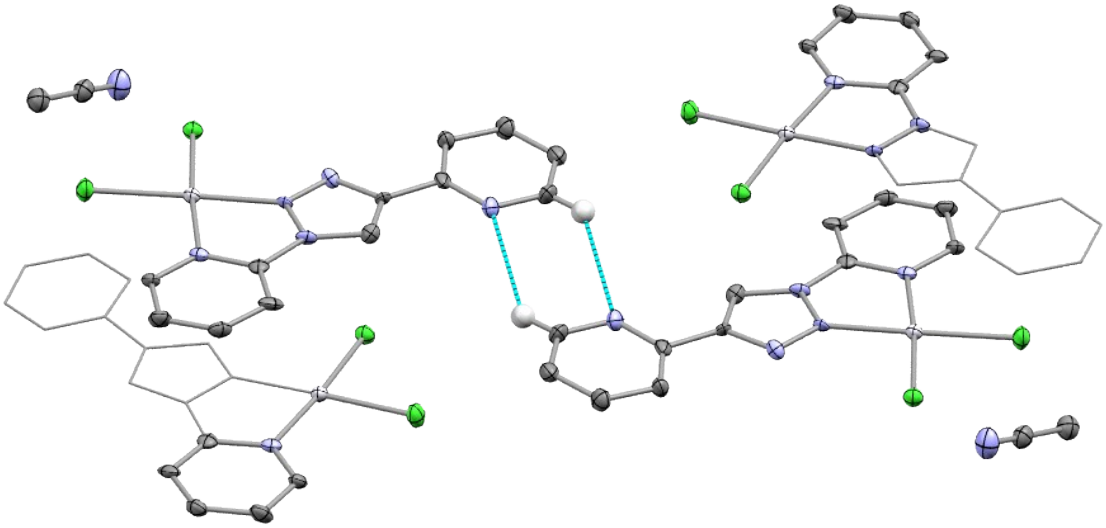

Figure S12 – Dimeric C-H···N interaction between two molecules of crystalline phase **3**.

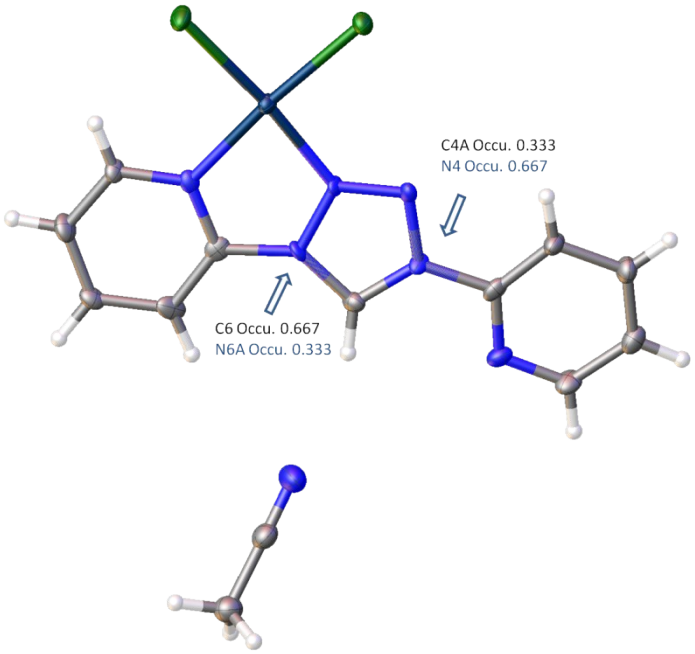

Figure S13 – X-Ray diffraction model of **3** showing disordered nature of N_1 and C_4 due to the *reg* and *inv* binding isomerism.

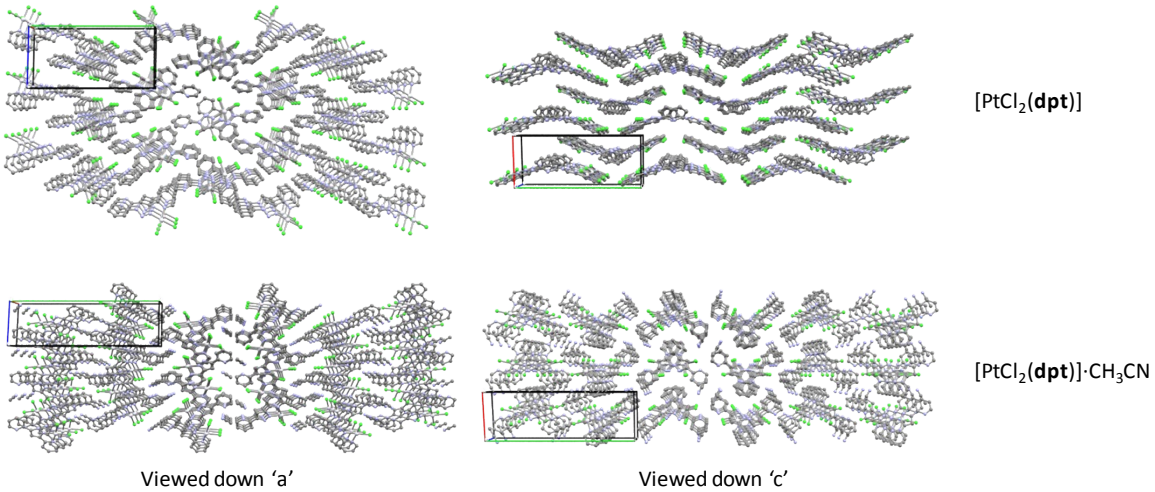

Figure S14– Packing diagrams of **2** (top) and **3** (bottom) showing difference in the final crystal packing geometries.

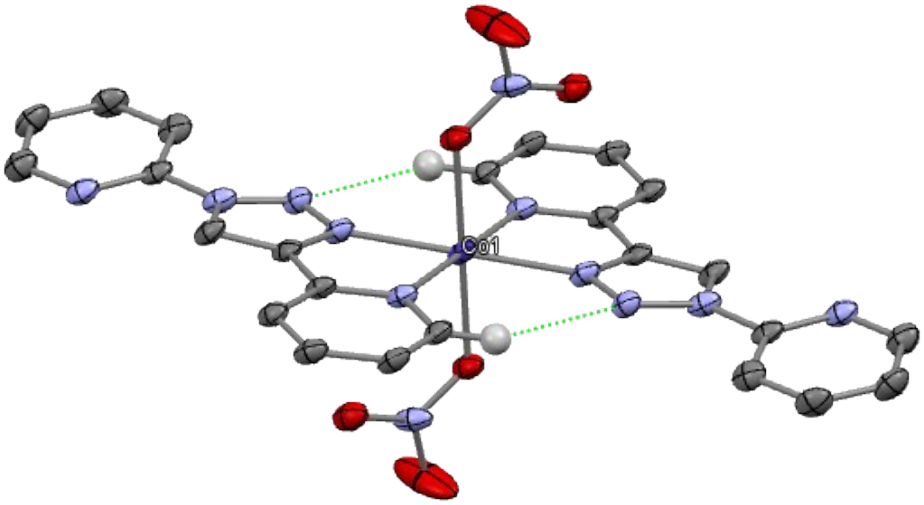

Figure S15 – Intramolecular C-H···N interactions in **4**.

X-ray powder diffraction

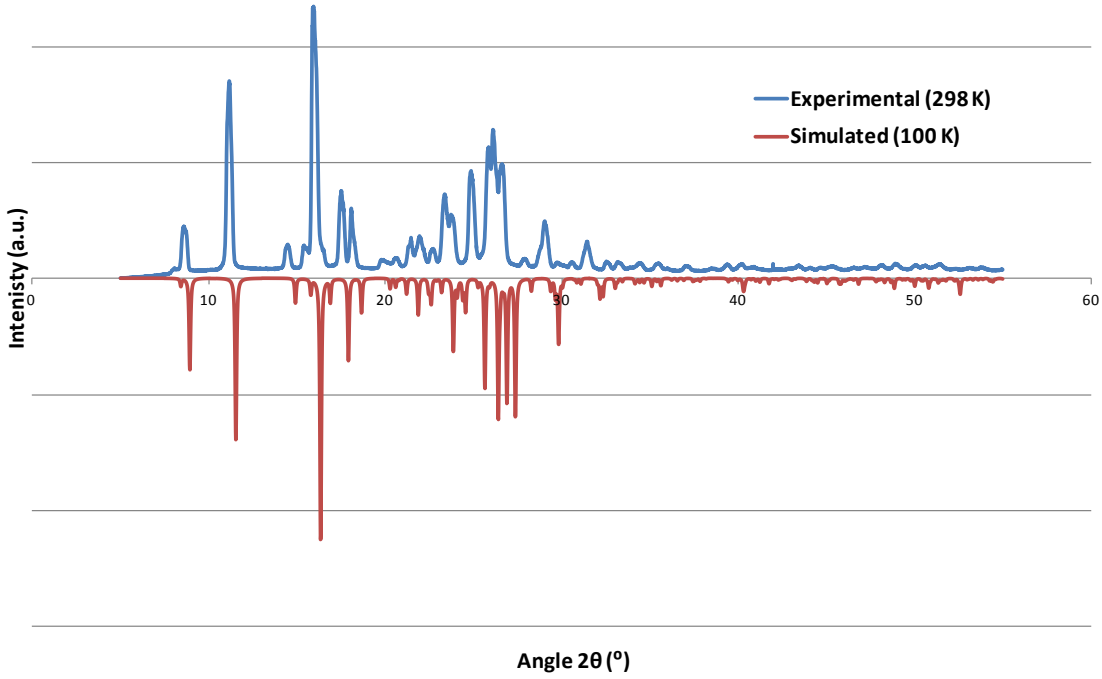

Figure S16 - X-ray powder diffraction pattern for **dpt**

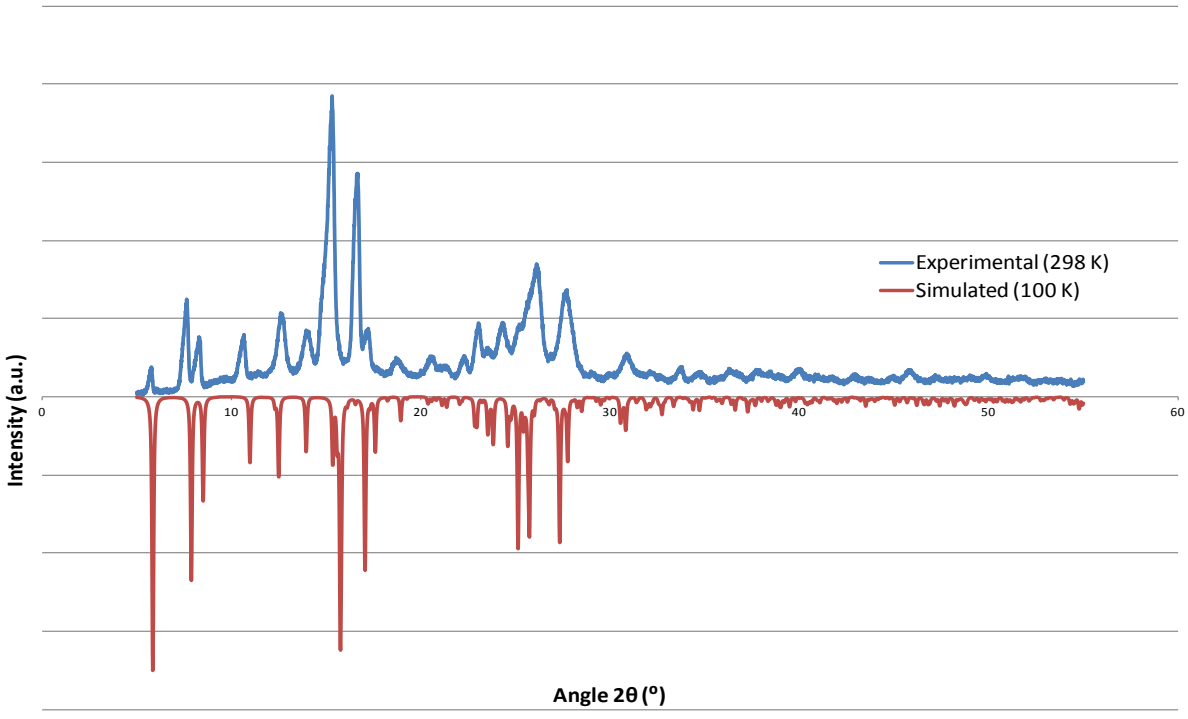

Figure S17 - X-ray powder diffraction pattern for **1**.

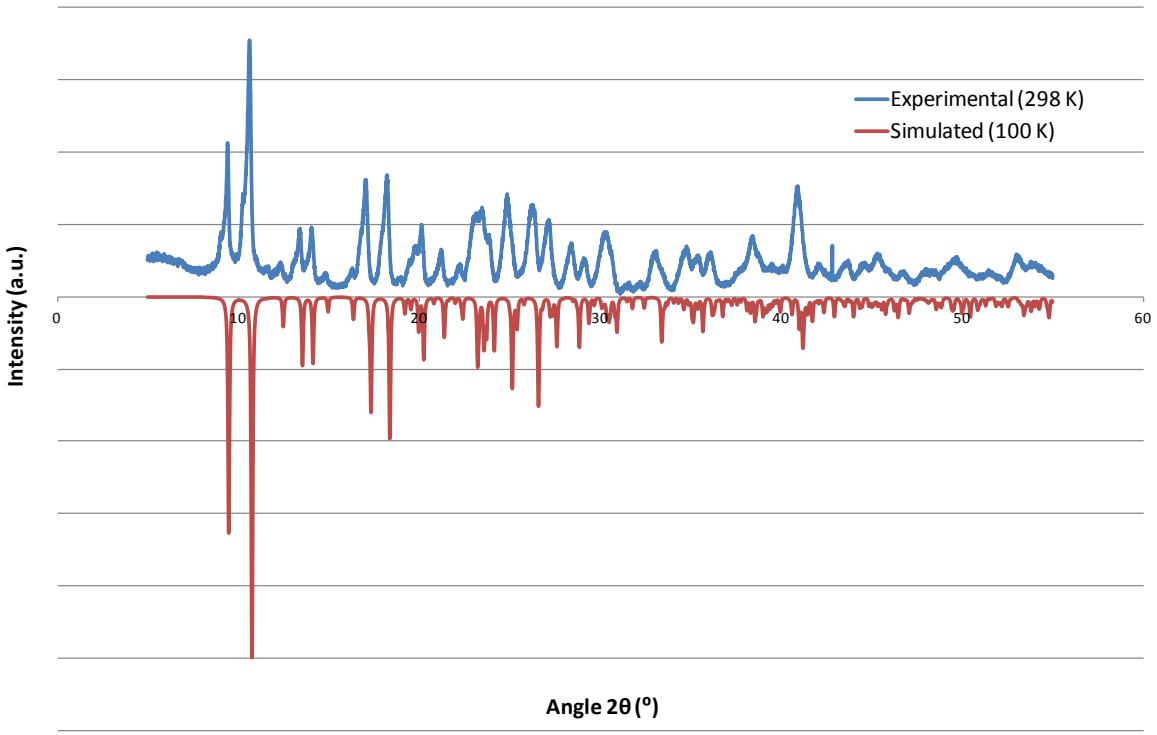

Figure S18 - X-ray powder diffraction pattern for **2**

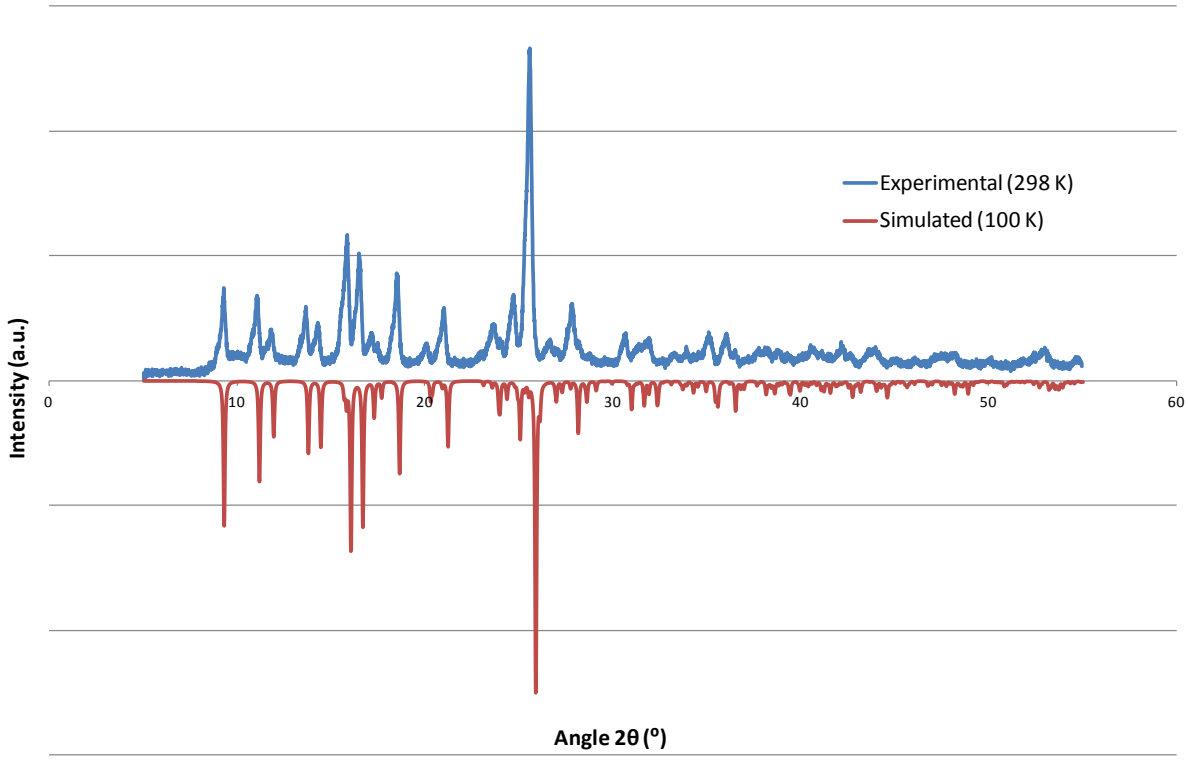

Figure S19 - X-ray powder diffraction pattern for **4**.

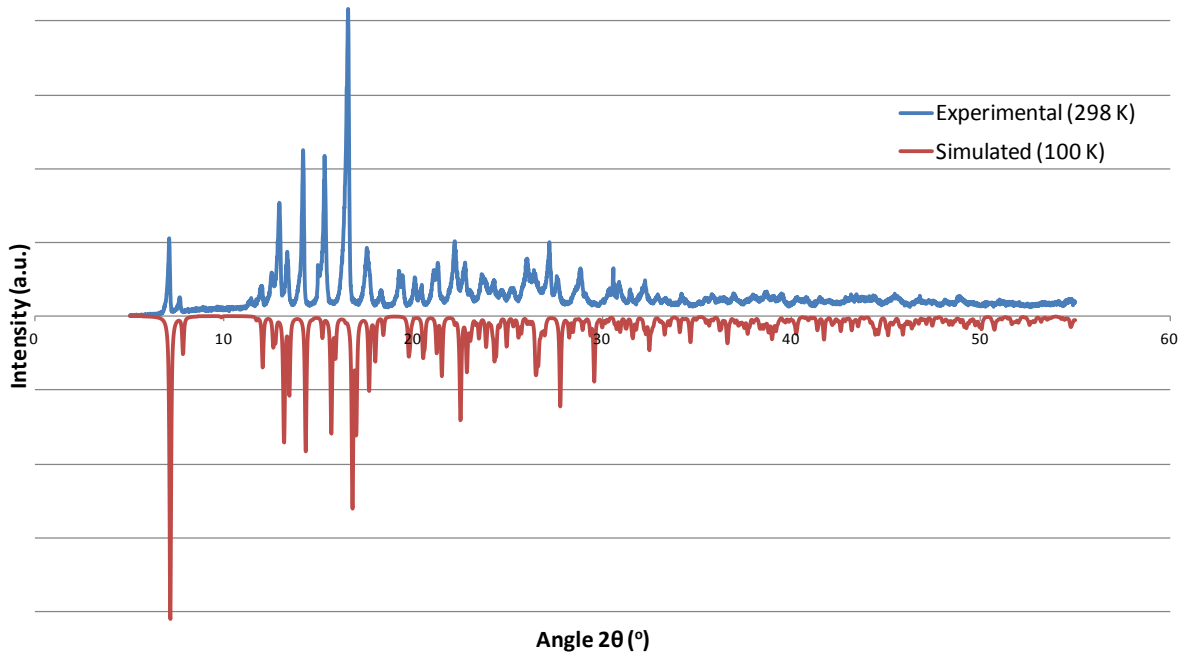

Figure S20 - X-ray powder diffraction pattern for **5**.

Crystallographic evidence for the selectivity of *reg* vs. *inv* binding

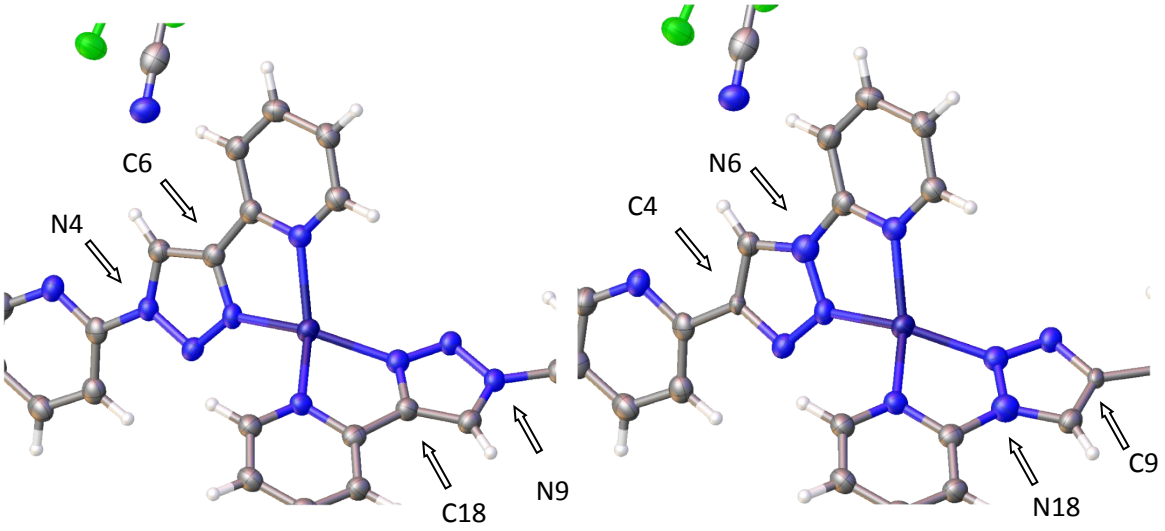

Figure S21 – Complex **1** modelled with Cu(I) in *reg* (left) and in *inv* (right) binding pocket.

	reg				*inv*			
R_1 ($I \geq 2\sigma$) / %	6.14				6.83			
U_{eq}	**N_4**	0.028	**N_9**	0.029	**N_6**	0.040	**N_{18}**	0.039
	C_6	0.029	**C_{18}**	0.028	**C_4**	0.019	**C_9**	0.020

Table S1 – Comparison of R_1 and U_{eq} for *reg* and *inv* models of **1**

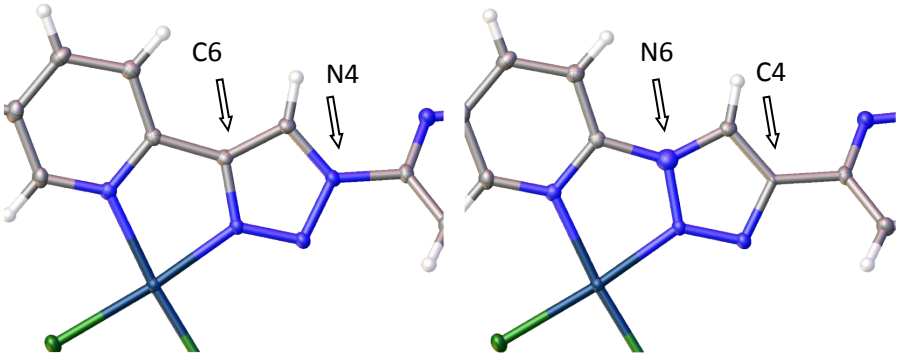

Figure S22 – Complex **2** modelled with Pt(II) in *reg* (left) and in *inv* (right) binding pocket.

	reg		*inv*	
R_1 ($I \geq 2\sigma$) / %	1.72		1.94	
U_{eq}	**N_4**	0.012	**N_6**	0.020
	C_6	0.011	**C_4**	0.005

Table S2 – Comparison of R_1 and U_{eq} for *reg* and *inv* models of **2**

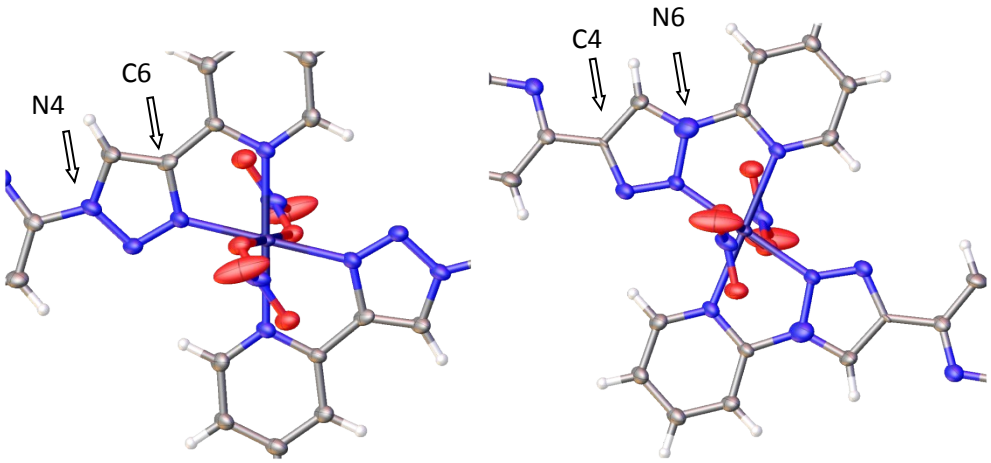

Figure S23 – Complex **4** modelled with Co(II) in *reg* (left) and in *inv* (right) binding pocket.

	reg		***Inv***	
R_1 ($I \geq 2\sigma$) / %	6.95		7.41	
U_{eq}	**N_4**	0.023	**N_6**	0.038
	C_6	0.023	**C_4**	0.011

Table S3 – Comparison of R_1 and U_{eq} for *reg* and *inv* models of **4**

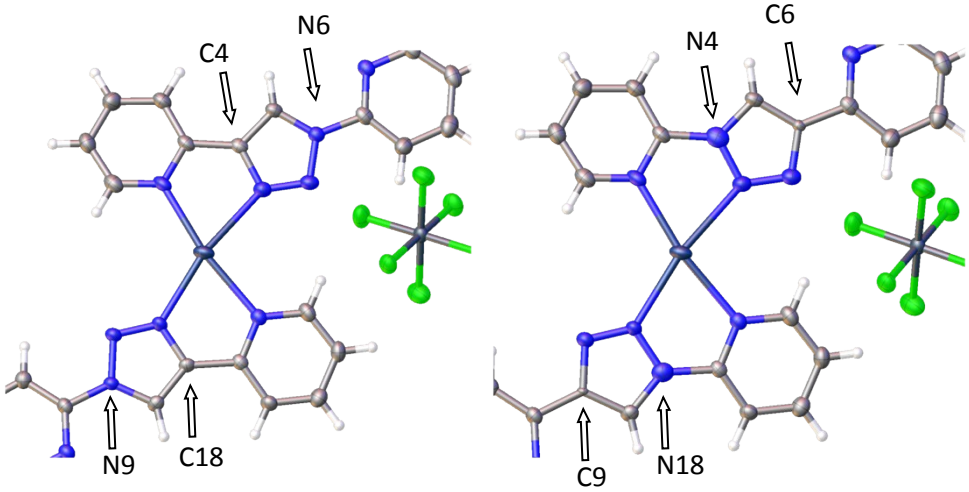

Figure S24 – Complex **5** modelled with Ag(I) in *reg* (left) and in *inv* (right) binding pocket.

	reg				***Inv***			
R_1 ($I \geq 2\sigma$) / %	4.19				4.51			
U_{eq}	**N_4**	0.022	**N_9**	0.018	**N_6**	0.032	**N_{18}**	0.030
	C_6	0.020	**C_{18}**	0.018	**C_4**	0.012	**C_9**	0.009

Table S4 – Comparison of R_1 and U_{eq} for *reg* and *inv* models of **5**

Residual Electron Density in Compound 3

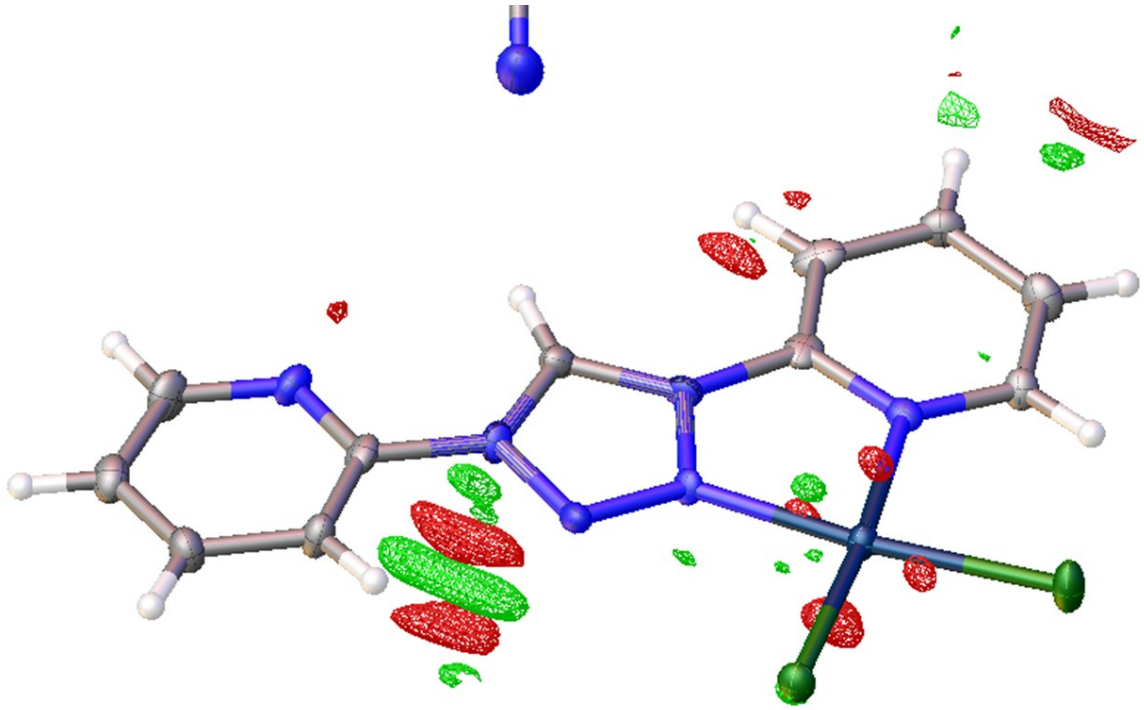

Figure S25 - Residual electron density map for compound **3** with residual surfaces rendered at ±1.35 e·Å^{-3}. Positive regions of $F_o^2 - F_c^2$ shown in red. Negative regions shown in green

Thermogravimetric Analysis

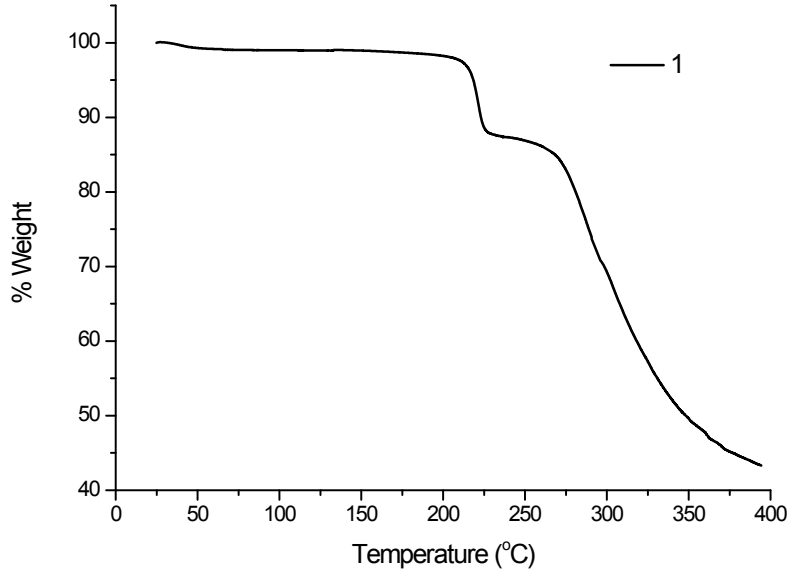

Figure S26 - Thermogravimetric Analysis for compound **1**.

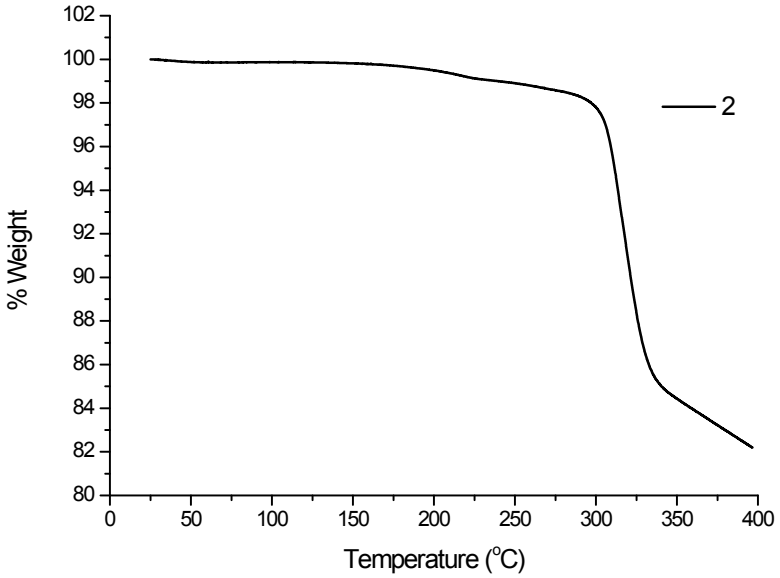

Figure S27 - Thermogravimetric Analysis for compound **2**.

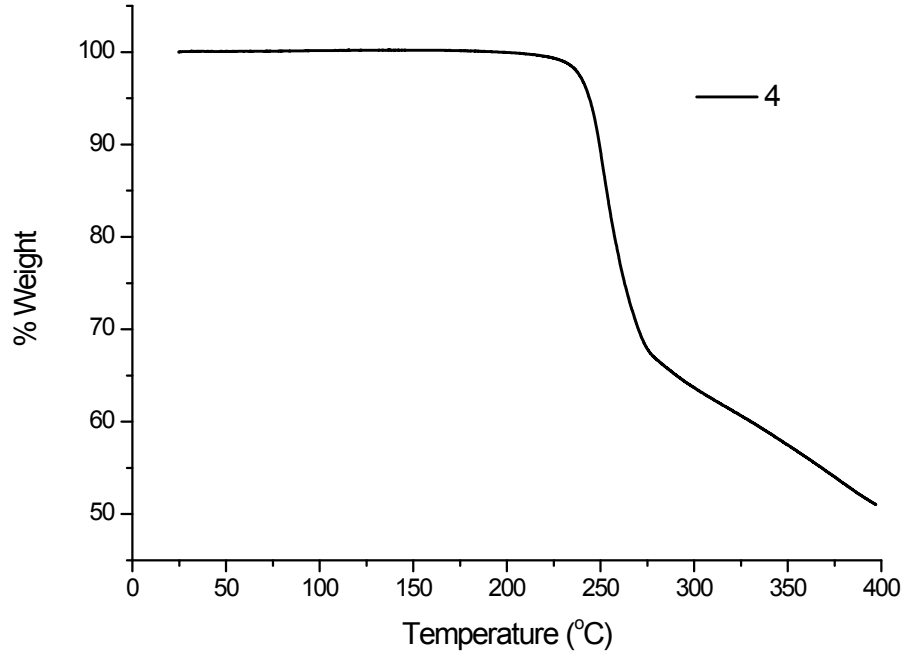

Figure S28 - Thermogravimetric Analysis for compound **4**.

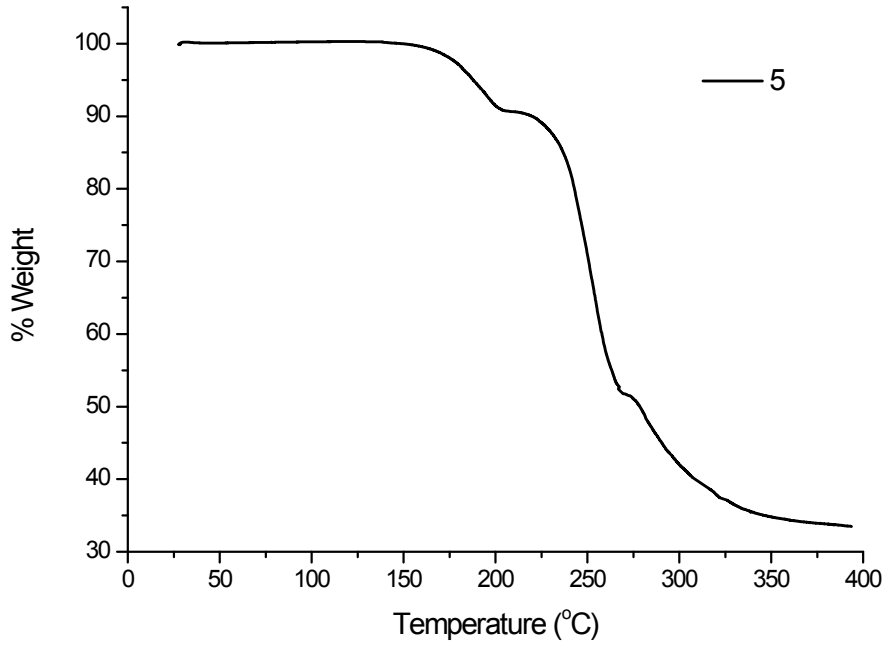

Figure S29 - Thermogravimetric Analysis for compound **5**.